fire

Article

Essential Organizing and Evolving Atmospheric Mechanisms Affecting the East Bay Hills Fire in Oakland, California (1991)

William Agyakwah [1,2], Yuh-Lang Lin [1,3,*] and Michael L. Kaplan [4]

1   Applied Science & Technology (AST) PhD Program, North Carolina A&T State University, Greensboro, NC 27411, USA; william.agyakwah@ertcorp.com
2   NOAA/NCEP/CPC/Earth Resources Technology, College Park, MD 20740, USA
3   Department of Physics, North Carolina A&T State University, Greensboro, NC 27411, USA
4   Division of Atmospheric Sciences, Desert Research Institute, Reno, NV 89512, USA; michael.kaplan@dri.edu
*   Correspondence: ylin@ncat.edu

Abstract: This study examined atmospheric mechanisms affecting the East Bay Hills Fire (1991) in Oakland, California, using the Advanced Weather Research and Forecasting (WRF) model and North American Regional Reanalysis (NARR) dataset. High-resolution WRF simulations, initially at 16 km, were downscaled to 4 km and 1 km for analyzing primary and secondary circulations at synoptic and meso-α/meso-β scales, respectively, before the fire. Additionally, the interaction between the synoptic-scale and mesoscale environments was examined using backward trajectories derived from NARR data. The findings reveal that a strong pressure gradient created by a ridge over the Great Basin and a trough off the Pacific coast generated favorable meso-α conditions for the hot, dry northeasterly winds, known as "Diablo winds", which initiated the wildfire in northern California. Mountain waves, enhanced by jet stream dynamics, contributed to sinking air on the Sierra Nevada's western slopes. The main conclusion is that jet circulation did not directly transport warm, dry air to the fire but established a vertical atmospheric structure conducive to wave amplification and breaking and downward dry air fluxes leading to the necessary warm and dry low-level air for the fire. The hot–dry–windy (HDW) fire weather index further confirmed the highly favorable fire weather conditions.

1. Introduction

Terrain-induced winds often lead to major wildfires in California [1–3]. Diablo, Santa Ana, and Sundowner winds have caused major wildfires such as the East Bay Hills Fire (1991), Cedar Fire (2003), and Sherpa Fire (2016), respectively. This study will focus on the orographic effects of Diablo wind on the East Bay Hills Fire [4]. Diablo wind is a hot and dry northeasterly wind that occurs in the San Francisco Bay area during the fall [5], similar to Santa Ana winds in Southern California. Diablo winds result from a high-pressure system over the great basin of the inland western states and an offshore low-pressure system that causes the wind to flow from northeast to southwest, decreasing relative humidity and increasing wind speed [6]. Similar to the East Bay Hills Fire (1991), the 2018 Camp Fire ignited during extreme weather, with low fuel moisture due to lack of rainfall. This dry landscape was prone to ignition. From November 7 to 9, a downslope windstorm acceler-ated the fire's spread, creating critical conditions for a destructive wildfire. This windstorm resulted from a mix of synoptic weather patterns, intensifying the fire's severity [7]. Also,

research indicated that in northern California, Diablo winds changed in strength and direction throughout the Tubbs Fire (2017) study [8]. Nevertheless, the complex landscape and fluctuating conditions led to unanticipated characteristics, including wind streaks and stagnation zones on the leeward sides of specific topographic formations. This complex airflow consistently mirrored the times, directions, and patterns of fire arrival, notably including lateral expansion when interacting with topographic features.

On Saturday, 19 October 1991, a small vegetation fire ignited in the Berkeley Hills near Grizzly Peak Boulevard, according to information from the Oakland Fire Department. The fire burned five acres before it was brought under control by the Oakland Fire Department and local agencies. This incident is associated with the East Bay Hills Fire of 1991. Crews monitored hotspots overnight despite challenging conditions. The fire was rekindled on Sunday, October 20, around 10:53 PDT (1753UTC), fueled by dry conditions and winds of 15 to 30 mph. Although firefighters were initially confident in controlling the fire, sparks spread rapidly through dry brush, expanding over a mile into Temescal Canyon. The fire was uncontrollable at 11:04 PDT (1804 UTC). Winds split the fire into two fronts, leading to the observation of flaming whirlwinds and fireballs. During the afternoon, the fire advanced through neighborhoods like Rockridge and Forest Park, moving about three-quarters of a mile and igniting wooden-roofed structures. By Sunday evening, firefighters started gaining control as winds calmed and temperatures dropped. The fire was halted by Monday morning, 21 October 1991, and mop-up operations began. After three days of intense efforts, the fire was fully extinguished, and crews worked to prevent new ignitions. Over 3354 single-family dwellings, 456 apartments, and 2000 cars were destroyed, making it the most expensive wildland–urban fire in US history at that time. Huang et al. [1] used data and simulations to study the synoptic-scale and mesoscale environment during the Cedar Fire (2003). They identified three stages of interaction: In stage I, dry air was transported from the upper troposphere to the surface due to a meso-alpha-scale subsidence region. In stage II, the jet streak intensified and caused strong northeast winds to move the dry air toward California's coast. In stage III, the interaction of a wave-induced critical level and strong upper-level sinking air motion led to the formation of Santa Ana winds. We will investigate whether a similar interaction occurred during the East Bay Hills Fire (1991) and whether a jet streak transported dry air to the surface. Huang et al. [1] used NHMASS data, while we used NARR data for backward trajectory. We aim to analyze synoptic-scale and mesoscale environments and test a new fire weather index (HDW) [9]. We calculated HDW using WRF simulated results to identify the days when meso-α scale weather activity contributed to the East Bay Hill Fire (1991). The HDW uses fundamental principles of observed favorable fire weather environment to identify the best meteorological variables that control wildfires at the synoptic and meso-alpha scales.

Srock et al. [9] introduced a new variable for assessing the risk of heat and drought waves (HDW) by combining atmospheric heat and moisture. The fire community commonly uses relative humidity (RH), which includes temperature as a variable. The vapor pressure deficit (VPD) variable is used to assess the amount of possible evaporation for HDW. A larger difference between e_s and e at a given temperature implies higher evaporation rates in plant environments. The VPD variable has been widely used in environmental science for assessing evapotranspiration rates [10–12].

$$VPD\ (T, q) = e_s(T) - e(q) \tag{1}$$

where *VPD* is the vapor pressure deficit, *T* is the temperature, *q* is the specific humidity as $e_s(T)$ is the saturation vapor pressure at temperature *T*, and $e(q)$ is the actual vapor pressure based on the specific humidity *q*. A larger (smaller) VPD directly correlates to a faster (slower) evaporation rate, which is, in turn, associated with a greater (lesser) potential for

the atmosphere to affect a fire. Hence, they propose the equation to calculate the HDW as wind speed (*U*) times the VPD:

$$HDW = U * VPD\ (T, q) \tag{2}$$

where *HDW* is the hot–dry–windy index, *U* is the wind speed, and *VPD* (*T*, *q*) is the vapor pressure deficit. Strong downslope winds are linked to wildfires, and their dynamics must be understood to manage and prevent related fires.

Two major mechanisms that intensify downslope winds are the resonant amplification mechanism [13] (hereafter referred to as CP84) and the hydraulic mechanism [14] (hereafter referred to as S85). CP84's mechanism is more in line with Klemp and Lilly [15] and Peltier and Clark [16], while S85's mechanism is more in line with Long [17] and Durran [18] and has been observed in the real atmosphere (e.g., [19]) and shown in recent numerical simulations (e.g., [20]). This study will investigate the formation mechanisms of downslope winds related to the East Bay Hills Fire (1991) using WRF simulation. The study will measure wave breaking with simulated winds and isentropes. Unlike Lin and Wang's [21] idealized simulation, this study uses actual simulated results. Most California wildfires occur due to strong downslope winds, like the Diablo wind, which caused the East Bay Hills Fire in 1991. The National Weather Service has a conceptual model explaining how Diablo winds cause wildfires (https://en.wikipedia.org/wiki/Diablo_wind (accessed on 12 August 2021)). Due to the rapid advancements in wildfire research, in addition to the studies referred to above, more recent research can be found in publications such as Gronoff et al. [22], Gillmann et al. [23], and Ma et al. [24].

Based on the conceptual model explained above for Diablo winds, we propose to enhance our understanding of the key processes that led to the mesoscale environment conducive to the formation of the East Bay Hills fire by addressing the following questions: (a) How does the high-pressure circulation over the Great Basin force the air to go over the Sierra Nevada? (b) Could the downslope motion be (i) enhanced by the sinking air motion associated with an upper-level jet streak [1] or (ii) produced by the resonant amplification mechanism [13] (CP84) and/or (iii) hydraulic jump mechanism [14] (S85)? and (c) Will the hot, dry, and windy air blowing from Sierra Nevada's downslope maintain the same thermodynamic characteristics over the Central Valley of California? This study aims to address these questions by utilizing analyzed data from the North American Regional Reanalysis (NARR) dataset, focusing on the interaction between the mesoscale and synoptic scale environments. We will employ the WRF model to investigate the hot, dry, and windy airmass affecting California's Central Valley. Both NARR and WRF will also aid in exploring the mechanisms behind the severe downslope winds in the western Sierra Nevada. Section 2 will cover the model description and experimental design, while Section 3 will focus on examining the synoptic and mesoscale environments favorable for wildfire occurrence. In Section 4, we will delve into the mechanisms of severe downslope winds on the lee slope of the Sierra Nevada. Next, Section 5 will analyze how the hot, dry, and windy air propagates across California's Central Valley and estimate HDW. Lastly, Section 6 will offer concluding remarks.

2. Simulation Methodology

The WRF model version 3.9 [25] was adopted for the East Bay Hills Fire (1991) numerical simulations in Oakland, California. The WRF model is a numerical weather prediction system designed to understand mesoscale weather phenomena better. To achieve this, the model incorporates either initial idealized data or real-time data for better operational weather prediction. WRF is a fully compressible, three-dimensional model that uses terrain-following vertical coordinates with stretched grid resolution. It also includes one-way or

two-way multiple nesting capability, along with a variety of options for upper and lateral boundary conditions. To test the ability of the WRF model to simulate the East Bay Hills Fire event, the methodology of Huang et al. [1] was employed. In their study, Huang et al. [1] analyzed the October 2003 extreme fire event in Southern California using the non-hydrostatic (NHMASS) version 6.3 of the Mesoscale Atmospheric Simulation System (MASS). We performed sensitivity tests utilizing data from the National Centers for Environmental Prediction (NCEP), NARR, and the European Centre for Medium-Range Weather Forecasts (ECMWF) to initialize the WRF model. Also, we chose the options for physics parameterization based on similar studies of wildfires in California [1,26].

Our findings indicate that the model initialized with ECMWF data is more precise than the other two datasets compared to the observed data. Although the ECMWF data aligned well with the observed data, a few errors were noted. The ECMWF sounding data showed that the winds changed from northeast to southwest 12 h earlier than the observed sounding data. We utilized the ERA-Interim reanalysis data from ECMWF for the control simulation to initialize the WRF model. The domain comprises three grids with varying resolutions: 16 km (D1), 4 km (D2), and 1 km (D3). We utilized two-way interactions to facilitate interactions among the lateral boundary conditions for the D1 domain (16 km) and nested grid two-way interactions at the D2 domain (4 km) and D3 (1 km) domains (Figure 1). D1 domain covers the western United States and part of Canada to reproduce the synoptic flow in which the mesoscale environment is embedded. The southwestern states, including California, Nevada, Utah, and Arizona, fall within the jurisdiction of the D2 domain. The purpose of the D3 domain is to collect data on the meso-β-scale characteristics of the airflow over the San Francisco Bay Area, which the fire has significantly impacted. The simulations for domains D1, D2, and D3 run in parallel, starting at 10/19/12Z, 10/20/00Z, and 10/20/12Z, respectively, and ending at 10/21/12Z. This approach mimics Huang et al.'s [1] study. To capture very fine vertical motions, we use a domain top of 10 hPa and 75 stretched vertical levels, and the domains have grid points of 260 × 277 (D1), 457 × 437 (D2), and 597 × 609 (D3). The time step intervals are 60, 15, and 3.7 s for domains D1, D2, and D3, respectively.
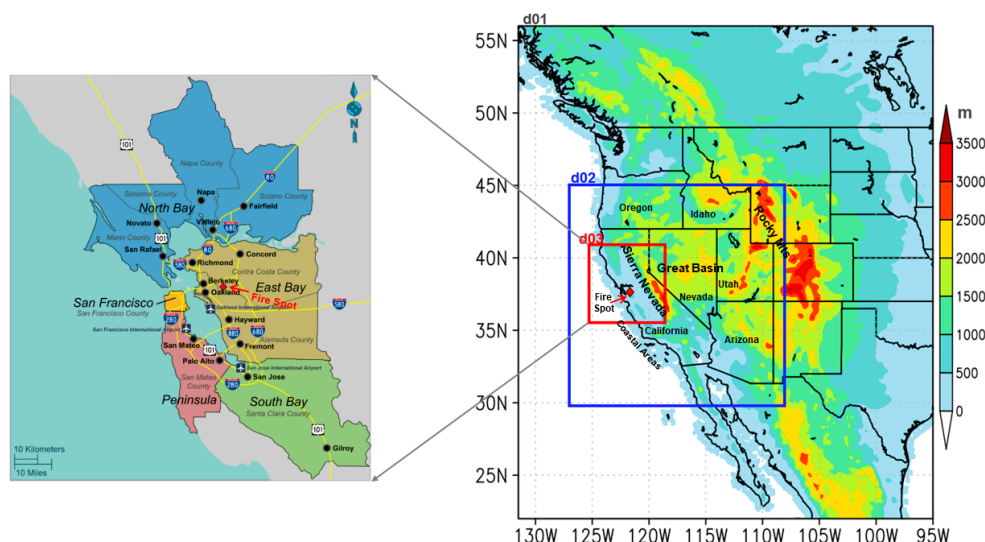

Figure 1. Domain set up for the East Bay Hills Fire (1991) with three nested domains with grid resolutions of 16 km (d01), 4 km (d02), and 1 km (d03). On the left-hand side is the zoomed-in view of the San Francisco Bay area and the East Bay Hills Fire location.

The simulations incorporate various options for physics parameterization, such as the Purdue Lin microphysics scheme [27], Kain–Fritsch cumulus scheme [28], Mellor–

Yamada–Janjic scheme for the planetary boundary layer [29], Rapid Radiative Transfer Model (RRTM) longwave radiation physics scheme [30], RRTM for General Circulations Models (RRTMG), and shortwave radiation physics scheme [31]. RRTM is the most precise for single-column calculations, while RRTMG is efficient with minimal loss of accuracy for General Circulation Model (GCM) applications. The Noah Land-Surface Model is the chosen land surface model. It is an all-in-one scheme developed by NCEP/NCAR/AFWA, featuring a four-layer soil temperature and moisture function, fractional snow cover, and frozen soil physics. The surface layer utilizes the Monin–Obukhov (Janjic Eta) similarity scheme, which is based on similarity theory and includes viscous sublayers over solid surfaces and water points.

3. Synoptic-Scale and Mesoscale Analyses

3.1. Synoptic Environment

During 19–20 October 1991, a strong upper-level ridge along the West Coast produced warm and dry weather conditions over northern California (Figure 2). Marine-layer clouds are low-altitude stratus clouds that form over the adjacent ocean waters. They are formed due to ocean water's cold surface temperatures, increasing air temperatures with height and producing temperature inversion. The air below the inversion is called the marine layer. The depth of the marine layer depends upon the large-scale weather patterns that pass high overhead. Marine-layer clouds often reach their maximum extent around sunrise, when the surface reaches a minimum temperature. The colder surface temperatures enhance the inversion layer and then increase the marine layer's depth.
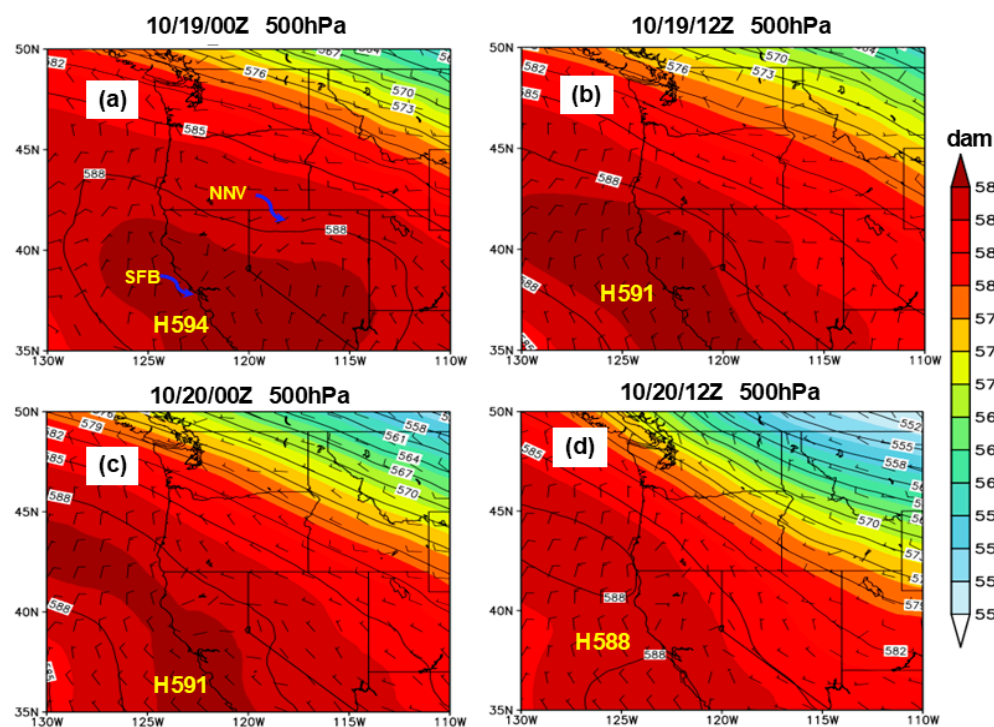

Figure 2. North American Regional Reanalysis (NARR) data of 500 hPa geopotential height (shaded) and wind barbs valid at (**a**) 10/19/00Z, (**b**) 10/19/12Z, (**c**) 10/20/00Z, and (**d**) 10/20/12Z. NNV indicates northern Nevada, and SFB is San Francisco Bay. The East Bay Hills Fire (1991) started on 20 October 1991, around 1753 UTC, peaked on October 20 between 1804 and 2000 UTC, and was extinguished in the morning of 21 October, around 0230 UTC.

Note that the sea breeze significantly affects the planetary boundary layer (PBL), the lowest part of the atmosphere where weather and air pollution occur. It forms during

the day as the land heats faster than the sea, generating winds that pull cool, moist air inland [32]. This cool air lowers the PBL height and reduces mixing, but turbulence at the sea breeze front can temporarily enhance it [33]. At the regional scale (D2 domain), factors like topography and weather systems impact the inland movement and reach of the sea breeze [34]. Locally (D3 domain), it causes sharp temperature, humidity, and wind changes, especially at its edge. In urban areas, it interacts with the urban heat island effect, leading to uneven changes in the PBL [35]. Ultimately, the sea breeze is crucial for influencing weather patterns, air quality, and cloud formation near coasts. In addition to the studies mentioned above, more recent literature can be found in publications such as Hinestroza-Ramirez et al. [36] and Heli et al. [37].

As the day progresses, sunlight penetrates the clouds and warms the surface and air above. This warming decreases the relative humidity of the cloudy air, and clouds begin to evaporate. Strong winds above the clouds can mix in drier air, leading to more evaporation, then the marine layer will dissipate [38]. The slow destruction of the marine layer gives rise to drier and warmer air near the coastal areas, and the increasing temperatures lower mean sea level pressures (MSLPs) along the coast. This lowering of MSLPs along the California coast produced an intensifying south to southwestward-directed pressure gradient across northern California through the weekend of 19 and 20 October (Figure 3). From the MSLP in Figure 3, the pressure difference between the San Francisco Bay (SFB) area and northern Nevada (NNV) was about 6–10 hPa from 10/19/00Z to 10/19/12Z. Twenty-four hours later, the MSLP along the California coast had fallen by 4 hPa or more. At the same time, the MSLP difference between the San Francisco Bay area and northern Nevada had increased to 10–14 hPa (Figure 3).
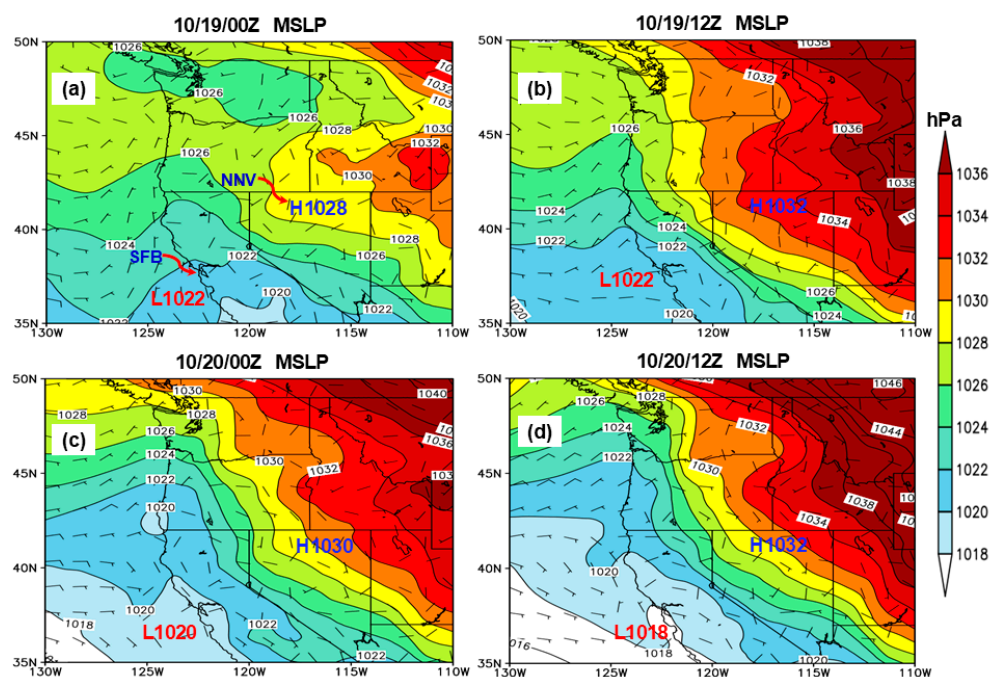

Figure 3. North American Regional Reanalysis (NARR) data of MSLP (shaded and contour lines; hPa) and wind barbs at (**a**) 10/19/00Z, (**b**) 10/19/12Z, (**c**) 10/20/00Z, and (**d**) 10/20/12Z. NNV indicates northern Nevada, and SFB is San Francisco Bay. The East Bay Hills Fire (1991) started on 20 October 1991, around 1753 UTC, peaked on October 20 between 1804 UTC and 2000 UTC, and was extinguished in the morning of October 21, around 0230 UTC.

The Oakland radiosonde ascent (Figure 4) indicates the presence of extremely dry air, which can be attributed to subsidence on 10/20/00Z. There was a low-level maximum of approximately 18 kts in the northeasterly wind at 4000 feet (approx. 900 hPa). During the

early morning, at 5:00 PDT 20 October (10/20/12Z), some marine air at the surface moved eastward near Oakland, but very dry conditions continued aloft, and the easterly winds increased (Figure 4). For the most part, over northern California, the MSLP continued to fall during the night until around 5:00 PDT on 20 October (10/20/12Z). During this period, the pressure difference between the San Francisco Bay area and northern Nevada reached a maximum of 14 hPa (Figure 3). The radiosonde data are sourced from the Wyoming sounding archive, which can be accessed at https://weather.uwyo.edu/upperair/sounding.html (accessed on 28 July 2021). This archive provides upper-air atmospheric profiles collected from radiosonde stations around the world. The data are obtained through the Global Telecommunications System (GTS), where various global radiosonde stations upload their observations. In the lower atmosphere, the vertical resolution is approximately 10 m. While sensor specifications, such as those from Vaisala RS41 and older models, may differ, local conditions can also slightly affect the levels of uncertainty in the data.
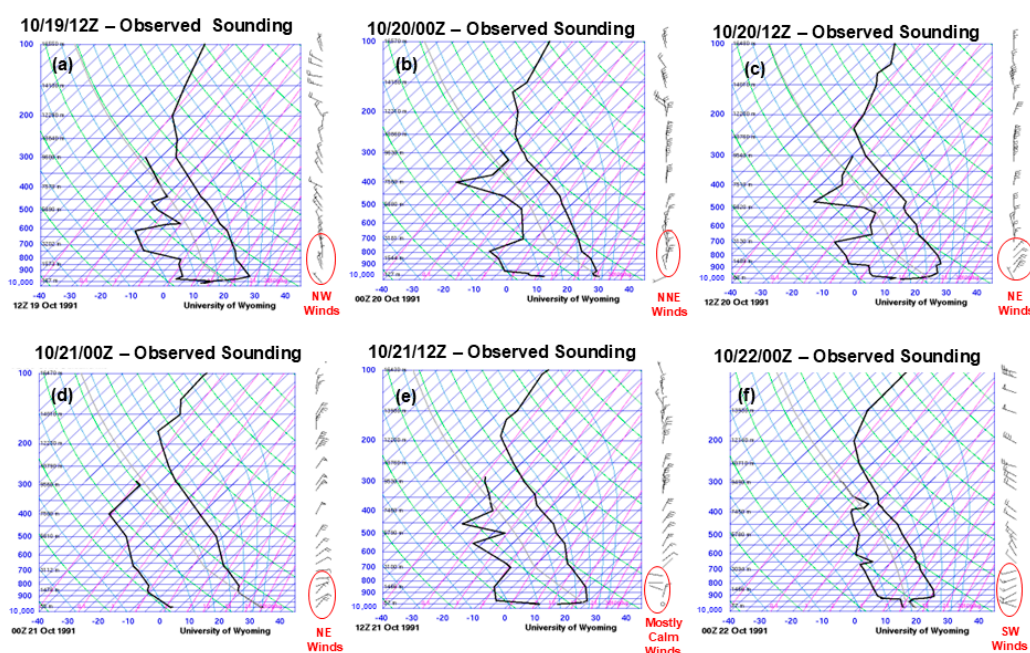

Figure 4. Observed thermodynamic diagram for Oakland International Airport valid at (**a**) 1200 UTC Oct 19 (10/19/12Z), (**b**) 10/20/00Z, (**c**) 10/20/12Z, (**d**) 10/21/00Z, (**e**) 10/21/12Z, and (**f**) 10/22/00Z. The solid lines on the left and right in each panel denote dewpoint temperature and temperature, respectively. The East Bay Hills Fire (1991) started on 20 October 1991, around 1753 UTC, peaked on October 20 between 1804 and 2000 UTC, and was extinguished in the morning of October 21, around 0230 UTC.

At 5:00 AM PDT on 20 October, a comparison was made between the 500 mb heights over San Francisco Bay and those from 19 October at 5:00 PM PDT. The results showed that the heights were lower due to the retrogression of the upper ridge. This retrogression supported more north-to-northeasterly flow at upper levels, as evidenced by Figure 4b,c. Consequently, the upper-level flow over the Great Basin became stronger. At the same time, the increasing Intermountain West MSLP gradient intensified the low-level winds generated by the low-level southwestward-directed/offshore pressure gradients. On 20 October at 11:00 AM PDT, the National Weather Service (NWS) reported that the shallow marine layer near Oakland's surface dissipated. This finding suggests that the observed changes in the 500 mb heights over San Francisco Bay from the previous day's measurements may have contributed to the dissipation of the shallow marine layer. The surface wind increased drastically, the temperature increased to ~13 °C in one hour (the highest temperature recorded for the day), and the dew point temperature fell to ~9 °C [39]. These phenomena

coincided with the initial blowup of the main fire complex at this time. The MSLP gradient lowered during the daytime as the northern Rockies and Great Basin surface pressures dropped. Eventually, as the MSLP gradient lowered around the San Francisco Bay (SFB) area, the support for northeasterly winds decreased during the day. Nevertheless, the strong winds continued in Oakland into the evening, and this can be seen in the observed Skew-T plot showing moderately strong winds (15–20 knots) at the surface and dissipation of the marine layer (Figure 4d). Afterward, the pressure gradient decreased, and the surface winds in the East Bay Hills area weakened substantially and turned to the west-northwest by 10/21/12Z (Figure 4e). Later, the west-northwesterly wind shifted to a southwesterly wind, causing a moist marine layer to enter the East Bay Hills fire area during the day, which helped lessen the fire (Figure 4f).

3.2. Mesoscale Environment

The WRF simulated 4 km resolution grid variables are used to analyze how hot, dry, and windy the environment was during the East Bay Hills fire. First, we investigate how windy it is using isotach plots at different levels and times. According to the Oakland Fire Department [6], the fire started at around 10:53 PDT (1753 UTC) on Sunday, 20 October 1991. The fire intensified on 20 October, between 1804 UTC and 2000 UTC. On 20 October, 19:30 PDT (0230 UTC, 21 October), the fire started diminishing as winds shifted from northeasterly to northwesterly. Concerning the start and end times, we analyze the WRF simulated data from 1200 UTC 19 October 1991 to 1200 UTC 21 October 1991. Figure 5 shows the wind speed at various levels during the fire event's start time (between 10/20/15Z and 10/20/18Z). At the fire location (denoted with a black dot), the winds from the surface up to 250 hPa are predominantly northeasterly. In connection with the observed Skew-T plot (Figure 4c,d), the winds are also northeasterly from the surface to about 200 hPa level during 10/20/12Z and 10/21/00Z, which the event's start time falls within. According to the simulated data obtained from WRF, the surface winds were moderately strong (12–14 ms^{-1}) from 10/20/15Z to 10/20/18Z, creating a highly favorable environment for the spread of fire (Figure 5).

Later, at the 850 hPa level, the northeasterly wind flow changed southwesterly (Figure 5), which advected moisture to the fire location at 10/21/12Z. Compared with the observed Skew-T plot, during 10/22/00Z from the surface to 700 hPa, the winds are primarily southwesterlies (Figure 4f). Although the southwesterly wind in the WRF simulation is seen earlier than in the observed Skew-T plot, both simulated and observed plots show similar wind directions during the start and end of the East Bay Hills Fire in Oakland. During 10/21/12Z, surface winds remain weak and variable, while southwest winds at 850 hPa introduce moisture to help extinguish the fire.

The RH profile near the fire site indicates a moist surface (RH at 60–70%) and drier conditions at 850 hPa on 10/20/15Z (Figure 6). This aligns with the presence of moist marine air near the surface, as depicted in the skew-T diagram (Figure 4d). Following the fire's intensification at 10/20/18Z, the surface humidity drops significantly to around 20–30%, with the 850 hPa levels also showing RH between 10 and 20% (Figure 6). Consequently, the atmosphere became dry from the surface to the 850 hPa level, fostering a supportive environment for wildland fire formation. The surface temperature rose consistently from 22 to 28 °C (72–82 °F) between 10/20/15Z and 10/20/18Z, as illustrated in Figure 7, which coincided with the wildland fire event's intensification. On 10/20/18Z, east of the fire location, the warm surface temperatures decreased from 30–34 °C to 24–30 °C (Figure 7). This is paralleled by a rise in surface relative humidity from 40 to 50% (Figure 6). The decrease in temperature and relative humidity increase can be partly linked to a change in

wind direction from northeast to southwest, facilitating moisture movement into the fire area and reducing the fire's intensity.
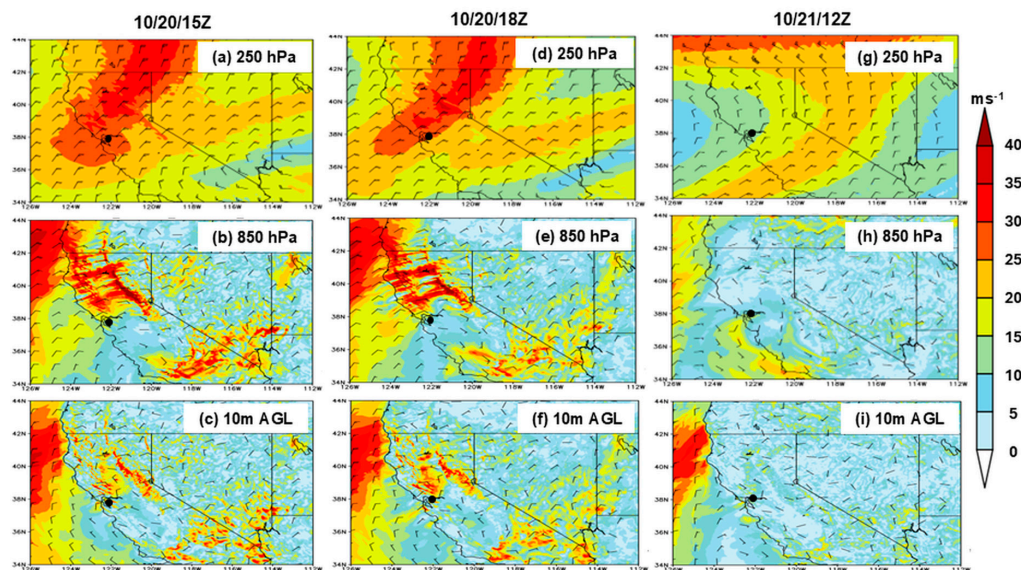

Figure 5. WRF (d02) simulated wind speeds (shaded; m s^{-1} and directions (wind barbs) at various levels during the fire event's start time between 10/20/15Z and 10/20/18Z, peak time between 10/20/18Z and 10/20/20Z, and extinguished the next day 10/21/12Z: 250 hPa (**a**), 850 hPa (**b**), and 10 m winds above the ground (**c**) at 10/20/15Z (left panels), 10/20/18Z (middle panels), and 10/21/12Z (right panels). Note that at the fire location (denoted with a black dot), the simulated winds from the surface up to 250 hPa are predominantly northeasterly (panels **a**–**g**) and moderately strong winds at the surface (12–14 ms^{-1}, panels **c**,**f**), which are consistent with those observed (Figure 4c,d) from 10/20/15Z to 10/20/18Z, creating a highly favorable environment for fire spread. The winds then turn to a south-southwesterly flow during 10/21/12Z (panels **h**,**i**), consistent with those observed (Figure 4e,f).
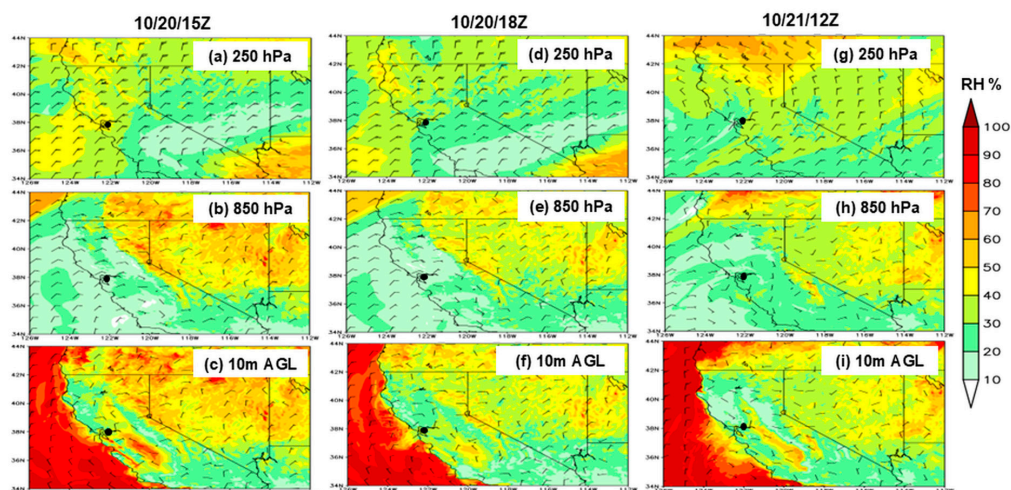

Figure 6. WRF (d02) simulated RH (shaded; %) and directions (wind barbs) at various levels during the fire event's start time between 10/20/15Z and 10/20/18Z, peak time between 10/20/18Z and 10/20/20Z, and extinguishing the next day 10/21/12Z: 250 hPa (**a**), 850 hPa (**b**), and 10m winds above the ground (**c**) at 10/20/15Z (left panels), 10/20/18Z (middle panels), and 10/21/12Z (right panels). Note that at the fire location (denoted with a black dot), the simulated winds from the surface up to 250 hPa are predominantly northeasterly (panels **a**–**g**). Additionally, near the fire site, the surface air was more humid (RH at 60–70%, panels **c**,**f**,**i**), but it was drier in the 850 hPa layer (RH at 10–20%, panels **b**,**e**,**h**), which indicates that the lower tropospheric air (surface to 850 hPa) advected drier air toward the ocean.
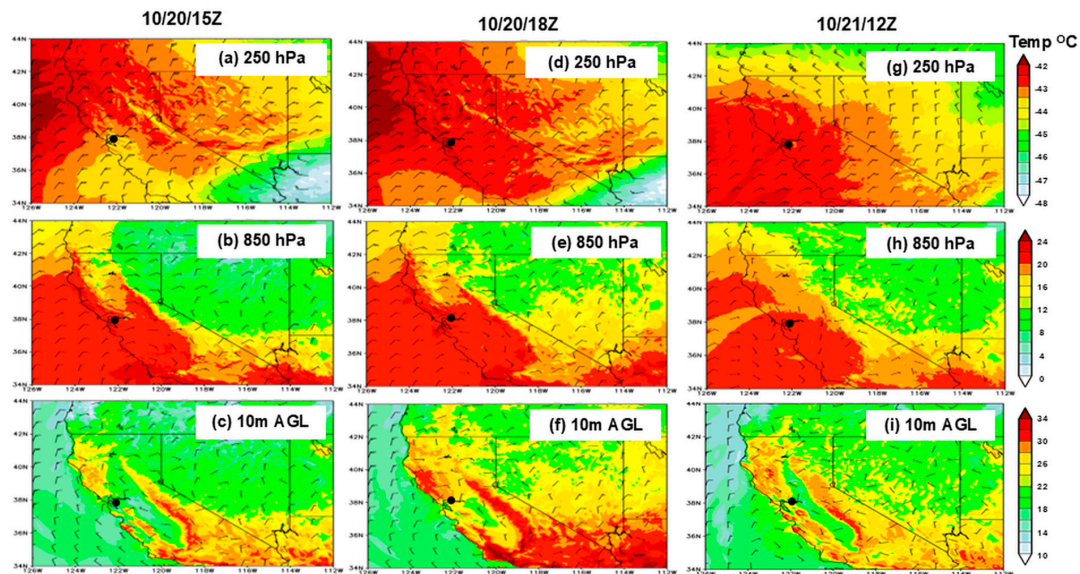
Figure 7. WRF (d02) simulated temperature (shaded; °C) and directions (wind barbs) at various levels during the fire event's start time between 10/20/15Z and 10/20/18Z, peak time between 10/20/18Z and 10/20/20Z, and extinguishing the next day 10/21/12Z: 250 hPa (**a**), 850 hPa (**b**), and 10 m winds above the ground (**c**) at 10/20/15Z (left panels), 10/20/18Z (middle panels), and 10/21/12Z (right panels). Note that at the fire location (denoted with a black dot), the simulated winds from the surface up to 250 hPa are predominantly northeasterly (panels **a**–**g**). Additionally, during the fire's start time, the surface temperature rose consistently from 24 to 32 °C (75–90 °F) (panels **c,f,i**), which helped to strengthen the fire intensity, with winds shifting to a south-southwesterly flow during 10/21/12Z (panels **h,i**), consistent with those observed (Figure 4e,f).

4. The Formation Mechanisms of Severe Downslope Winds over the Lee Slope of Sierra Nevada

The synoptic-scale and mesoscale environment interaction is examined using backward trajectories from the NOAA Hybrid Single Particle Lagrangian Integrated Trajectory (HYSPLIT) model [40,41]. The HYSPLIT model is a complete system for computing simple air parcel trajectories and complex transport, dispersion, chemical transformation, and deposition simulations. It is used for back trajectory analysis to determine the origin of air masses and establish source–receptor relationships. This study used the HYSPLIT model to compute the East Bay Hills fire trajectory at a particular location (37.86 N, 122.22 W) and date (10/18/12Z) where and when the fire occurred, respectively. We first discuss trajectories to indicate that air from the jet streak does not directly impact the fire location but does so indirectly by creating a more favorable mountain wave genesis and amplification environment. The trajectories are all initialized with NARR data starting at 1500 UTC 20 October 1991 (Figure 8a) and 1800 UTC 20 October 1991 (Figure 8b). They all end at 1200 UTC 18 October 1991. We use the backward trajectory analysis to describe the air parcels' source arriving at the location of interest.

Figure 8 shows the backward trajectory source at the fire location (37.86 N, 122.22 W), denoted with a star. The air parcel's origin is tracked during 10/20/15Z (Figure 8a) and 10/20/18Z (Figure 8b) to identify the air source that aided in the wildland fire. At 10/18/12Z, the air moves northwest at ~830 hPa and continues to move northwest until 10/18/18Z, when the air starts to move northeast, and its pressure falls to a minimum of about 750 hPa at 10/19/00Z (Figure 8). The air keeps moving northeast, and its pressure (750 hPa) is maintained until 10/20/00Z, when its direction changes to northerly. During this time, the air pressure increases sharply and reaches a maximum of 995 hPa at 10/20/09Z, and that same pressure is maintained till 10/20/18Z. In summary, the source

of the air was northwest during 10/18/12Z–10/18/18Z, it changed to northeast during 10/18/18Z-10/20/00Z, and finally during 10/20/00Z–10/20/18Z, it changed to north. The northeast parcel motion corresponds with the hot, dry, and windy airflow directed toward the East Bay Hills area.
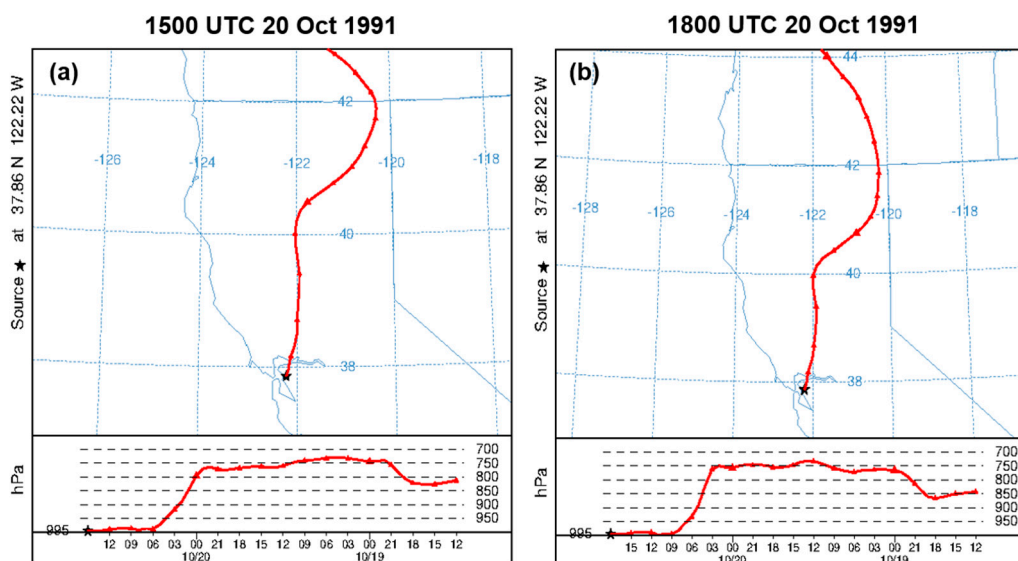

Figure 8. Backward trajectory analysis of air parcels from the NARR meteorological data starting from the fire location (37.86° N, 122.22° W) starting at (**a**) 1500 UTC Oct 20 (10/20/15Z), 1991, and (**b**) 10/20/18Z, 1991. They all end at 10/18/12Z, 1991. The analysis indicates that both air parcels near the East Bay Hills originated from northeast, at a level around 850 hPa, where the air was hot, dry, and windy. See text for detailed explanation.

From the backward trajectory analyses, we suggest the air parcel was dry, and its source is not from the jet streak, considering the minimum pressure of ~730 hPa. We further analyzed the formation mechanisms related to the severe downslope winds over Sierra Nevada's lee slope. We used a cross-section from the WRF simulation that passes through the jet streak's right-exit region and the fire location (Figure 9). We selected when the fire started, intensified, and decreased to determine whether the downward motion from the jet streak directly influenced the sinking motion at the East Bay Hills' lee side. Figure 9 shows that the jet streak's downward motion is far from the fire location. This may not directly affect the East Bay Hills' lee side's downward motion. Huang et al.'s [1] study found that northeasterly winds from the right exit region of the jet streak directly enhanced the severe downslope winds. The difference is that we hypothesize that the jet streak right exit region creates a different wave organizational environment, i.e., vertical structure, in conjunction with the jet streak circulation above the Sierra Nevada. According to the general theory of straight jet streak (for example, the straight jet streak conceptual model, e.g., [42]), upper-level divergence is found on the right entrance and left exit regions of the jet streak, and upper-level convergence is found on the left entrance and right exit regions of the jet streak. Where convergence occurs in the upper levels, sinking motion results; where divergence occurs in the upper levels, rising motion results [43] (Figure 3). This explains why the wind from the right exit region of the jet streak is dry and warm, changing the vertical structure of the stability and wind shear above Sierra Nevada.

To control wildfire events associated with severe downslope winds, there is a need to understand the basic mountain wave amplification dynamics. The understanding can be gained from the two principal mechanisms, (a) the resonant amplification mechanism [13] (CP84) and (b) the hydraulic mechanism [14] (S85), as proposed by Lin [44]. These two

mechanisms are applied in this study to understand the behavior of the severe downslope winds which induced the East Bay Hills fire.
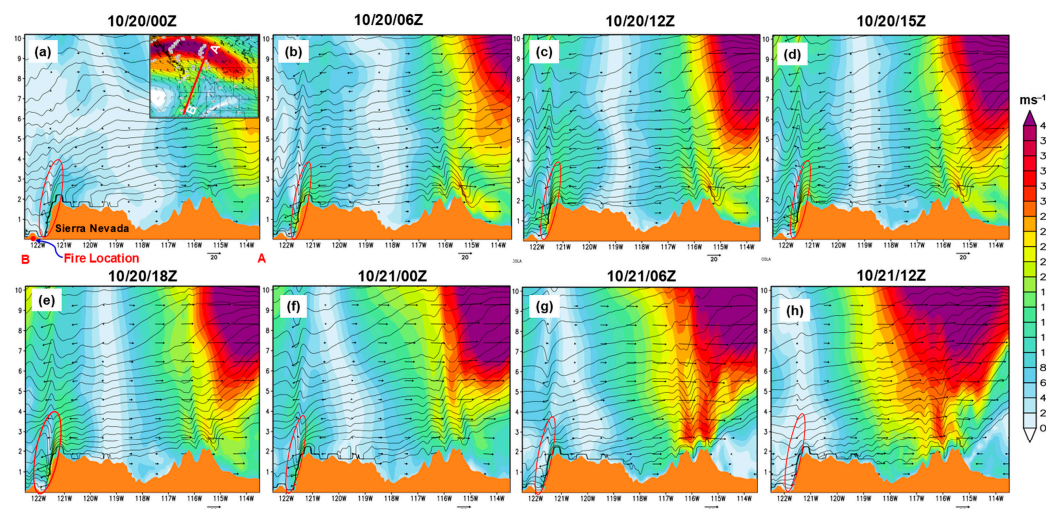

Figure 9. Cross-section along AB (denoted in the upper-right corner) from the WRF (d01) simulation of wind speeds (shaded; ms^{-1}), isentropes (contour lines; K), and wind barbs from 10/20/00Z to 10/21/12Z, 1991, for every 6 or 3 h, as shown on top of each figure panel (**a**–**h**). The cross-section line passes through the jet streak's right exit region and the fire location at 250 hPa level. This analysis indicates that downward motion associated with the jet streak at the exit region is far from the fire location (**a**–**h**). Thus, the downslope wind on the lee side of East Bay Hills did not seem to be affected by the jet streak directly.

First, we investigate the resonant amplification mechanism by examining the three distinct stages for forming severe downslope winds that Scinocca and Peltier [45] found. The first stage in their study involves local static (buoyancy) instability. This instability occurs when the wave steepens and overturns, resulting in a pool of well-mixed air aloft. Our study focuses on the severe downslope mechanism at the lee side of the Sierra Nevada. Figure 10 shows the wave steepening at around 2 km over the Sierra Nevada's slope during 10/20/06Z. As a result of this wave steepening, local static instability occurs, leading to waves overturning and forming a pool of well-mixed air aloft. The well-mixed region can be identified by large turbulent kinetic energy (TKE), visible at 10/20/06Z (Figure 10c).

The second stage is a well-defined large-amplitude stationary disturbance formed over the lee slope. Afterward, small-scale secondary Kelvin–Helmholtz (K-H) (shear) [46] instability develops in local regions of enhanced shear associated with flow perturbations caused by the large amplitude disturbance. From our WRF simulated results at this stage, we observe the well-mixed layer deepening, evidenced by an increase in the TKE at 10/20/09Z (Figure 10c). Also, the internal hydraulic jump's depth becomes greater, and the hydraulic jump (HJ) forms over the lee slope, as seen at 10/20/09Z (Figure 10a).

The third stage is on the lee slope. The enhanced wind region expands downstream and eliminates the perturbative structure linked with the large amplitude stationary disturbance. Using the WRF simulated results of this study, we observe that after the formation of a hydraulic jump, severe downslope winds develop at the lee slope during 10/20/15Z and 10/20/18Z (Figure 10a). As per Lin's research [44], the K-H instability is the primary factor controlling the flow during a windstorm's mature stage. Static instability, however, plays a crucial role in initiating a wave-induced critical level at the beginning stage and facilitating the downstream expansion of the severe winds on the lee slope.
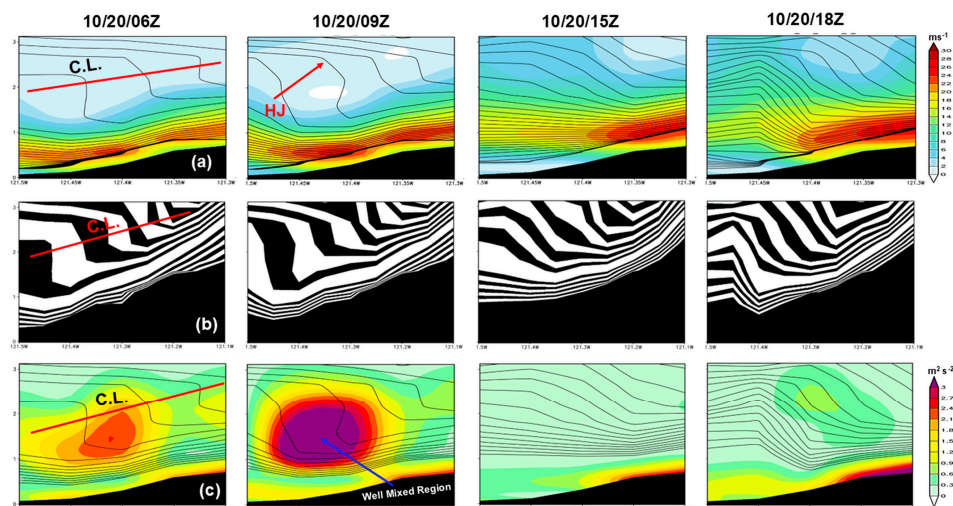
Figure 10. Vertical cross-section at the lee side of Sierra Nevada using the WRF (d02) simulation of (**a**) isotachs (shaded; m s^{-1}) and isentropes (contour lines; K), (**b**) isentropes (shaded; K), and (**c**) TKE (shaded; m^{2}s^{-2}) and isentropes (contour lines; K) from 10/20/06Z to 10/20/18Z. CL and HJ represent critical level and hydraulic jump, respectively. Note that the three distinct stages for forming severe downslope winds, as proposed in the resonant amplification mechanism [13,38], and the hydraulic jump and well-mixed (dead) region, as proposed in the hydraulic jump mechanism [14], can be identified in this analysis. Detailed discussions can be found in the relevant text.

In Figure 11, the vertical cross-section goes through the Sierra Nevada on the right-hand side and the East Bay Hills on the left-hand side. You can see the vertical cross-section profile in the upper-left corner. The red dashed lines indicate where wind reversal occurs, also known as the wave-induced critical level. The critical level (CL) is where the mean wind speed and the wave's phase speed coincide. The CL corresponds to the wind reversal level for a stationary mountain wave because the phase speed is zero (U = 0). Therefore, in the WRF output, CL is calculated by setting U = 0. The two blue horizontal lines show the CL heights calculated using the resonant amplification (z_c—upper) and the hydraulic (z_c and z_s—lower and upper) mechanisms.

Based on the resonant amplification mechanism by CP84 [13], the lowest wave-induced critical level starts to develop at height $z = 3\lambda_z/4 + n$. Using the WRF simulated results, the lowest wave-induced critical levels at times 10/20/03Z, 10/20/06Z, 10/20/09Z, 10/20/15Z, 10/20/18Z, 10/20/21Z, 10/21/00Z, and 10/21/03Z are 1585, 2651, 3199, 3554, 5159, 4925, 3621, and 1709 m, respectively (Figure 11). The CL height is estimated by first calculating the hydrostatic vertical wavelength (λ_z).

$$\lambda_z = 2\pi U/N \tag{3}$$

where U is the wind speed (ms^{-1}), and N is the Brunt Vaisala Frequency ($N = \sqrt{\frac{g}{\theta}\frac{\partial\theta}{\partial z}}$). On the other hand, the hydraulic mechanism predicts CL heights falling within the range of $z = 3\lambda_z/4 + n$ to $3\lambda_z/4 + n$ (n is an integer) [14] (S85). Since the CL height falls within a range, it is represented by the two (2) blue horizontal lines. From the WRF simulated results, the CL height at $z = \lambda_z/4 + n$ at times 10/20/03Z, 10/20/06Z, 10/20/09Z, 10/20/15Z, 10/20/18Z, 10/20/21Z, 10/21/00Z, and 10/21/03Z are 528, 884, 1066, 1185, 1720, 1642, 1207, and 570 m, respectively.

On 10/20/03Z, the wave above the slope steepens due to instability and then overturns and breaks to form a critical level (CL) (Figure 11a). According to CP84 [13], the wave-breaking region aloft acts as an internal boundary that reflects the upward propagating waves to the ground and produces the severe-wind state through partial resonance with

the upward propagating mountain waves. Similarly, the WRF simulated results show this phenomenon from 10/20/06Z to 10/20/18Z. At 10/20/06Z, wave breaking is evidenced by wind reversal on top of it. Below the wave-breaking region, there is severe downslope wind over the lee slope of Sierra Nevada. Afterward, the depth of the internal hydraulic jump increases (Figure 11b,c). The lower layer flow is more disturbed than the flow above the initial wave-induced critical level (seen at 10/20/09Z). Subsequently, severe downslope winds are formed through resonance between the upward and downward waves during 10/20/15Z and 10/20/18Z (Figure 11d,e). This period coincides with when the East Bay Hills fire started and indicated the effect of severe downslope winds that generated the wildfire. Furthermore, considering where the critical level forms, both mechanisms can identify where the severe wind state exists. Thus, with CP84 [13], the severe wind state will develop if the critical level is located at a height of $z = 3\lambda_z/4 + n$, while in S85 [14], the severe wind state exists over the whole range of critical level height between $z = \lambda_z/4 + n$ and $3\lambda_z/4 + n$ (n is an integer).
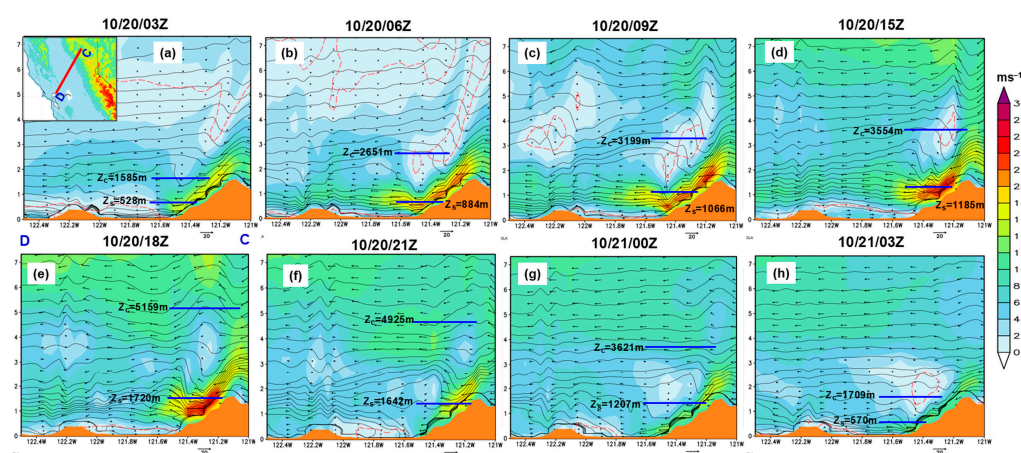

Figure 11. Cross-section along line CD (indicated in the upper-left panel) from the WRF (d02) simulation of isotachs (shaded; ms^{-1}), isentropes (contour lines; K), and wind barbs. The red dashed lines represent the level where wind reversal occurs. The two horizontal lines are critical level heights calculated using CP84's resonant amplification (upper) and S85's hydraulic mechanisms (upper and lower). This analysis implies that the resonant amplification and hydraulic jump mechanisms were responsible for the severe downslope wind formation in the wildfire event in Oakland, California. The panels illustrate the fire's ignition, escalation, and eventual extinction. The establishment of critical level (**a**) prompted the emergence of a wave breaking (**b**). The depth of the internal hydraulic jump increases (**c**), followed by the formation of intense downslope winds through resonance (panels **d**,**e**). Eventually, these winds diminished, and weaker winds are observed on the leeside of the Sierra Nevada, coinciding with the period when the fire was contained (panels **f**–**h**). Detailed discussions can be found in the text.

At the severe downslope winds stage (Figure 11d,e), strong winds are seen at the lee side of the Sierra Nevada, which transports the hot and dry air over the Central Valley of California to the East Bay Hills area (Figures 12 and 13). This process corresponds with when the East Bay Hills fire was uncontrollable at 11:04 PDT (1804 UTC) on 20 October 1991 [6]. The WRF simulation with a 1 km resolution (Figure A1) provides more details on how strong winds are transported over the lee slope of Sierra Nevada towards the East Bay Hills area. Figure A1 shows that the East Bay Hills Fire (1991) was caused by the resonant amplification and hydraulic jump mechanisms that resulted in downward motion at East Bay Hills. This implies that the resonant amplification and hydraulic jump mechanisms were responsible for the tragic event in Oakland, California.
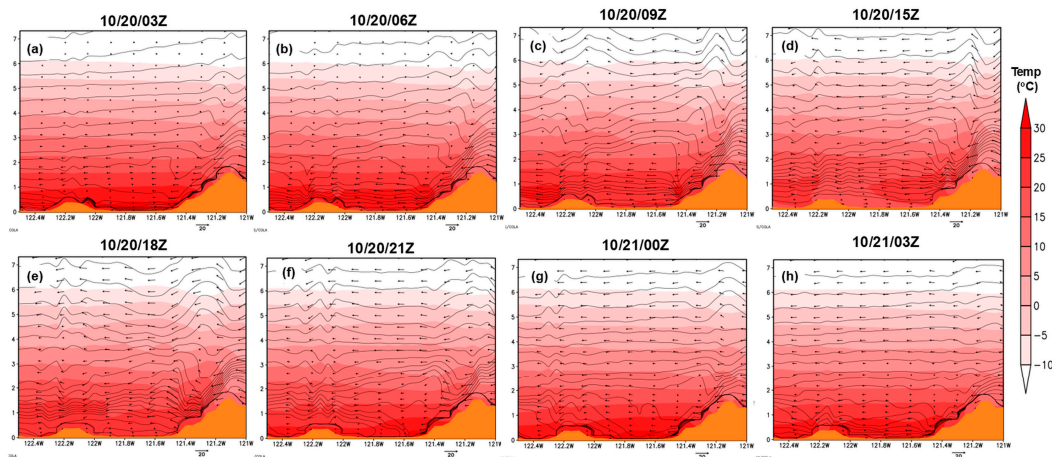
Figure 12. Cross-section along line CD (denoted in Figure 11) from the WRF (d02) simulated temperature (shaded; °C), isentropes (contour lines; K), and wind barbs from 10/20/03Z to 10/21/03Z. Note that the high-temperature layer near the surface (**a**,**b**) at the Central Valley became relatively colder than the air above (~2 km) (**c**–**e**), due to the sinking air motion associated with the high-pressure system extending southwestwards from the Great Basin offshore decreases the depth of the marine layer. Panels (**f**–**h**) illustrate that wind speeds decreased, revealing weaker winds on the leeside of the Sierra Nevada when the fire was contained. Refer to the text for a more detailed discussion.
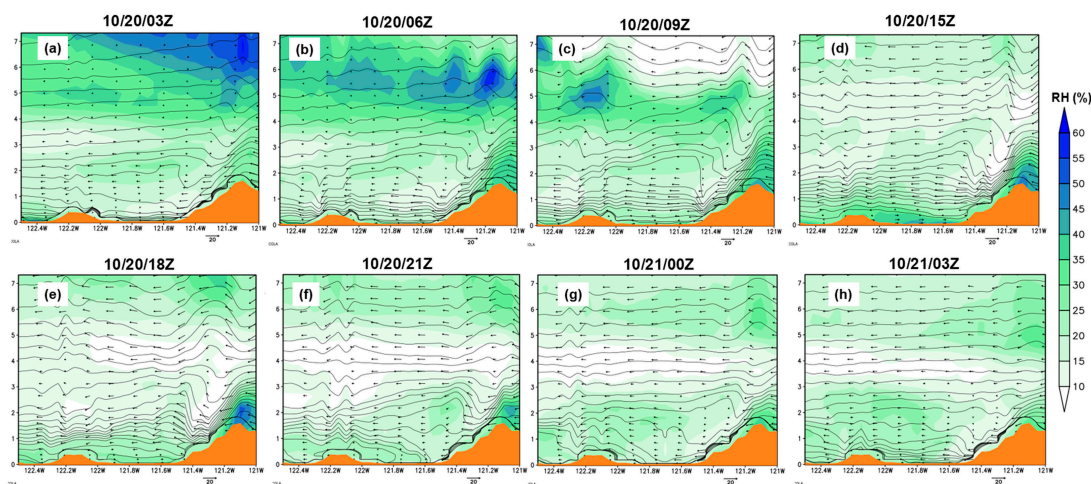

Figure 13. Cross-section along line CD (denoted in Figure 11) from the WRF (d02) simulated RH (shaded; %), isentropes (contour lines; K), and wind barbs from 10/20/03Z to 10/21/03Z. Along with Figure 12, the sinking air motion associated with the high-pressure system extending southwestwards from the Great Basin offshore leads to the destruction of the marine boundary layer and then a warmer and drier air at the surface. Strong winds are seen at the lee side of the Sierra Nevada, which transports dry air over the Central Valley of California to the East Bay Hills area (Panels **a**–**e**). Panels (**f**–**h**) illustrate that wind speeds decreased, revealing weaker winds on the leeside of the Sierra Nevada when the fire was contained. See detailed discussions in the text.

5. Propagation of Hot, Dry, and Windy Air over the Central Valley of California

Once Sierra Nevada wave mechanisms have created a hot, dry, and windy airmass, the propagation of this airmass over the Central Valley of California is investigated using the WRF simulated results. One of the objectives of this study is to determine whether the hot, dry, and windy air from Sierra Nevada's downslope retains the same characteristics over the Central Valley. We used temperature, relative humidity (RH), and isotach plots to investigate this objective.

From the temperature plots, the vertical cross-section of the WRF simulation shows high temperatures > 30 °C close to the surface at the Central Valley area from 10/20/03Z to 10/20/06Z (Figure 12a,b). From 10/20/09Z to 10/20/18Z, the air temperature becomes relatively colder at the surface than the air aloft (about 2 km above the surface), which could be related to the moist marine air layer (Figure 12c–e). As described in the synoptic overview in Section 3, the sinking air motion associated with the high-pressure system extending southwestwards from the Great Basin offshore decreases the depth of the marine layer. This destruction leads to warmer and drier air at the surface, as seen in Figures 12 and 13. The WRF simulated temperature and RH at a high 1 km resolution clearly shows the warm and dry surface during the fire event over and near the Bay region (Figures A2 and A3). In addition, in Figure 13, we see that RH ranges between 30 and 50% at the Central Valley's surface during 10/20/09Z and 10/20/15Z. Later, from 10/20/18Z, the RH decreased below 30% when the fire started and kept falling on time. One significant finding is that around 10/20/15Z, the cold air at the surface behaves like a virtual mountain (stable layer) linking the Sierra Nevada and East Bay Hills. Thus, the hot, dry, and windy air passed over the virtual mountain to the coastal mountain range (Figures 12 and 13). The virtual mountain phenomenon is also seen in the 1 km resolution of the WRF simulation of RH (Figure A3).

With the wind speed decrease, there is a wave-induced critical level above the lee side of Sierra Nevada at 10/20/03Z, leading to mixing during 10/20/06Z and 10/20/09Z. Later, HJ features form, which produces severe downslope winds from 10/20/15Z to 10/20/18Z (Figures 11 and A1). This hot, dry, and strong downslope wind creates favorable conditions for wildfire, resulting in the fiery conflagration at the East Bay Hills. The above analysis shows that the hot, dry, and windy air from Sierra Nevada's downslope maintains the same characteristics over the Central Valley and intensifies when it passes over the East Bay Hills' lee side.

Estimate of Hot–Dry–Windy (HDW) Index

The mesoscale analysis from the WRF simulation shows that the atmosphere was windy, dry, and hot, which are some of the key meteorological variables needed for wildfires to occur [47]. To diagnose more details about the meso-α scale weather activity that caused the East Bay Hills Fire (1991), we calculate the HDW (explained in Section 1) using the WRF simulation (4 km resolution—d02). For the East Bay Hills Fire event, the WRF simulation results show that the high HDW index is located between the surface and 800 m level. Due to this, we selected the highest wind speed and vapor pressure deficit (VPD) from any level in the lowest 800 m to the surface, unlike Srock et al. [9], who used the layer from the lowest 500 m to the surface. We calculated HDW using our WRF simulated results by following the same approach Srock et al. [9] used in calculating their HDW. In Figure 14, the HDW is shown a few hours before the fire started through the time it abated. At 10/20/15Z, the highest HDW occurred at the fire location (black shaded circle). This high HDW set the pace for favorable wildfire conditions, which started around 10:40 PDT (1740 UTC) on 20 October 1991. At the southeastern and especially southwestern part of the fire location, there is high HDW, and this indicates how the fire moved and affected areas like Berkeley (west), Oakland City (east), Piedmont (southeast), and other nearby cities. In addition, the high HDW at the southwestern part of the fire location shows the winds were predominantly northeasterly, which moved the fire to the southwest of the fire location. Afterward, HDW decreased with time at the fire location until 17:00 PDT on October 20 (10/21/00Z). At 20:00 PDT October 20 (10/21/03Z), the HDW increased again, most likely due to daytime heating. Afterward, the HDW decreased again up to the end of the simulation period (Figure 15).
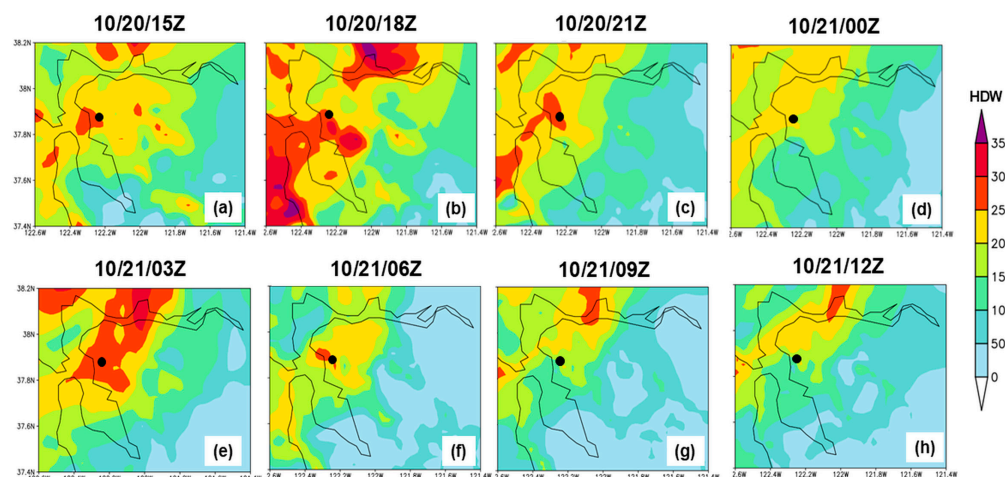
Figure 14. Maximum HDW (shaded) using WRF (d02) simulated data from 10/20/15Z to 10/21/12Z. The black dot indicates the fire location (122.22 W, 37.86 N). Note that the highest HDW occurred at the fire location (black shaded circle) on 10/20/15Z (**a**), which set the pace for a favorable wildfire that started around 10/20/1740Z (**b**). This high–HDW created favorable conditions for the wildfire, which ignited around 10:40 PDT (1740 UTC) on 20 October 1991. The elevated HDW indicates how the fire spread and affected Berkeley and surrounding areas. Subsequently, HDW gradually decreased at the fire location until 17:00 PDT on 20 October (10/21/00Z) (**c**,**d**). At 20:00 PDT on the same day (10/21/03Z) (**e**), the HDW increased again, likely due to daytime heating. Following this, the HDW diminished once more, coinciding with the time the fire was contained (**f**–**h**).
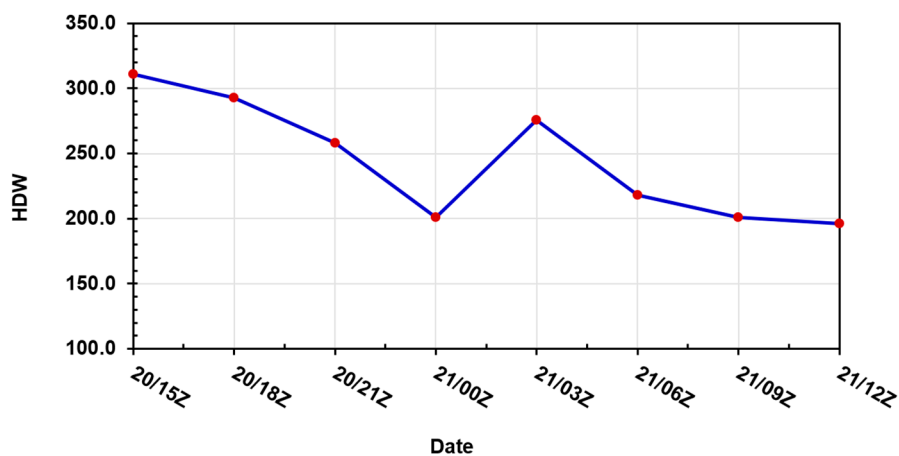

Figure 15. Time series of the HDW using WRF (d02) simulated data at the fire location (122.22 W, 37.86 N) from 10/20/15Z to 10/21/12Z. Along with Figure 14, the high HDW set the pace for favorable wildfire conditions, which started around 10/20/1740Z, 1991. At 10/21/03Z, the HDW increased again due to daytime heating. Later, the HDW reduced until the end of the simulation period.

6. Discussion and Conclusions

6.1. Discussion

This study tried to understand the basic atmospheric mechanisms responsible for the East Bay Hills fire (1991) in Oakland, California. In doing so, we examined the conceptual model proposed by the National Weather Service (https://en.wikipedia.org/wiki/Diablo_wind (accessed on 12 August 2021)) which explained how the Diablo wind formed and produced the wildfire in northern California. We analyzed observational data using NARR datasets and numerical simulations using the WRF model.

Based on our analyses of observed and numerical simulated data, we found a strong upper-level ridge along the West Coast, which induced warm temperatures and dry weather

conditions over northern California on 19 and 20 October 1991. Sinking air related to the high pressure decreased the marine air layer thickness, leading to drier and warmer air along the coastal areas. On the other hand, the increasing temperatures induced low MSLP along the coast and produced a strong north-to-northeast pressure gradient across northern California. The strong pressure gradient was evidenced by the pressure difference increasing from 6 to 14 hPa between the San Francisco Bay area and northern Nevada during 10/19/00Z and 10/20/12Z. The strong pressure gradient forced northeasterly winds to accelerate toward the coastal mountain ranges in northern California. Also, cold air advection over the Great Basin supported sinking air motion over the lee side of Sierra Nevada.

We also analyzed whether the local downward motion was directly coupled with the sinking air motion associated with an upper-level jet streak. We tested this issue using the NOAA HYSPLIT model's backward trajectory code. The results indicate that the source of the air parcels that caused the severe winds on the lee side of the East Bay Hills was not directly from the jet streak, considering the minimum parcel pressure of 730 hPa. Instead, the jet streak's right exit region indirectly enhanced downward motion at the lee side of the Sierra Nevada by establishing a favorably discontinuous vertical atmospheric structure above the Sierra Nevada. This structure favored mountain wave amplification and downslope wind formation. The wave-induced descending Sierra Nevada lee side air dried, warmed, and interacted with warm air in the Central Valley. This ensemble airmass of dry and warm air was advected downstream. It generated severe downslope winds at the East Bay Hills' lee side, created hydraulic jump features, and caused wildfire in the East Bay Hills area of Northern California. Our further investigation was conducted using a vertical cross-section of the WRF simulation. The results show that the jet streak's sinking motion was far from the fire location and might not directly influence the East Bay Hills' lee side's downward motion. We used a vertical cross-section from the WRF simulation to confirm these findings. The results demonstrated that the jet streak's sinking motion was too distant from the fire location to directly influence the downward motion over the East Bay Hills. Instead, the jet streak enhanced atmospheric conditions that favored wave amplification and breaking and downward dry air fluxes, resulting in the necessary warm and dry low-level air for the fire.

6.2. Conclusions

This study investigated the atmospheric mechanisms contributing to the East Bay Hills Fire (1991), focusing on the role of resonant amplification [13] (CP84) and hydraulic jump mechanisms [14] (S85) as proposed by Lin [44], in producing severe downslope winds over the East Bay Hills lee slopes. Our results verified that this mechanism developed hot, dry, and windy conditions conducive to fire formation. Furthermore, we explored the movement of hot, dry, and windy air originating from the lee side of the Sierra Nevada, which maintained its characteristics as it traveled across the Central Valley and intensified upon reaching the lee side of the East Bay Hills.

Using the HDW (hot–dry–windy) index approach proposed by Srock et al. [9], we analyzed the predictability of the East Bay Hills Fire event. Our findings indicated that the highest HDW values occurred on 10/20/15Z, creating conditions favorable for rapid fire spread, which peaked around 10/20/18Z. Subsequently, HDW values decreased until 10/21/03Z before rising again during the daytime heating period. The HDW index patterns closely aligned with the fire spread and abatement timeline, reinforcing its potential as a predictive tool for fire behavior.

Additionally, we highlighted the role of complex terrain and canyons influencing the East Bay Hills Fire dynamics. These findings underscore the need for further studies to analyze the sensitivity of such features to atmospheric mechanisms. This study acknowledges

limitations in the spin-up period and nesting ratio selection. Our analysis' lack of a spin-up period may limit the initialization; future work will include an appropriate duration for better model results. Furthermore, we will refine the 1:4 nesting ratio, which may cause interpolation errors, using an odd ratio (e.g., 1:3) to improve numerical consistency.

Future research can leverage idealized large eddy simulations (LES) using the WRF model, possibly supplemented by enhanced canyon-scale observational networks, to gain deeper insights into the interplay of terrain, wind patterns, and fire behavior.

In summary, our work provides a foundation for understanding the atmospheric dynamics that contributed to the East Bay Hills Fire (1991) and emphasizes the importance of integrated modeling and observational approaches for improving fire predictability in complex terrains.

Author Contributions: W.A. contributed to writing, computation, and visualization. Y.-L.L. and M.L.K. contributed to the conceptualization and funding acquisition. All authors have read and agreed to the published version of the manuscript.

Appendix A

Further figures provide insights into the transport of strong winds over the lee slope of the Sierra Nevada toward the East Bay Hills using data on the meso-β-scale airflow characteristics collected over the San Francisco Bay Area, which are mainly influenced by the fire.
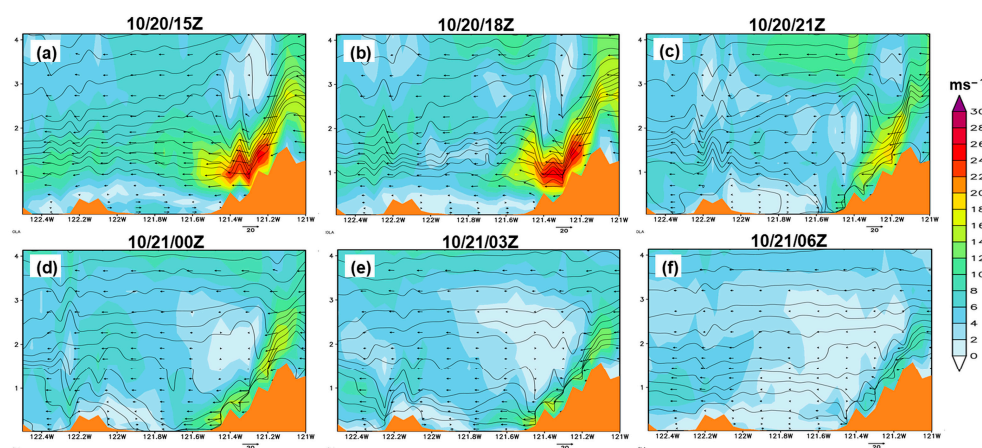

Figure A1. Vertical cross-section from the WRF (d03) simulation of isotachs (shaded; ms^{-1}), isentropes (contour lines; K), and wind barbs from 10/20/15Z to 10/21/06Z. The cross-section is along line CD (denoted in Figure 11). The establishment of critical level prompted the emergence of a wave breaking. The depth of the internal hydraulic jump increases followed by the formation of intense downslope winds through resonance (panels **a**,**b**). Eventually, these winds diminished, and weaker winds are observed on the leeside of the Sierra Nevada, coinciding with the period when the fire was contained (panels **c**–**f**).
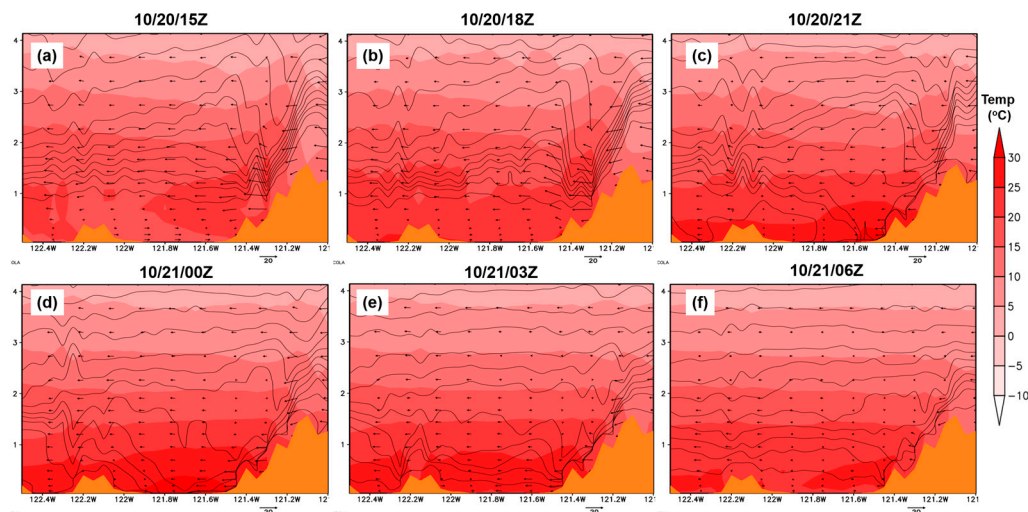
Figure A2. Vertical cross-section from the WRF (d03) simulation of temperature (shaded; °C), isentropes (contour lines; K), and wind barbs from 10/20/15Z to 10/21/06Z. The cross-section is along line CD (denoted in Figure 11). Note that at the Central Valley temperatures became relatively colder than the air above (~2 km) (**a**,**b**), due to the sinking air motion associated with the high-pressure system extending southwestwards from the Great Basin offshore decreases the depth of the marine layer. Panels (**c**–**f**) illustrate that wind speeds decreased, revealing weaker winds on the leeside of the Sierra Nevada when the fire was contained.
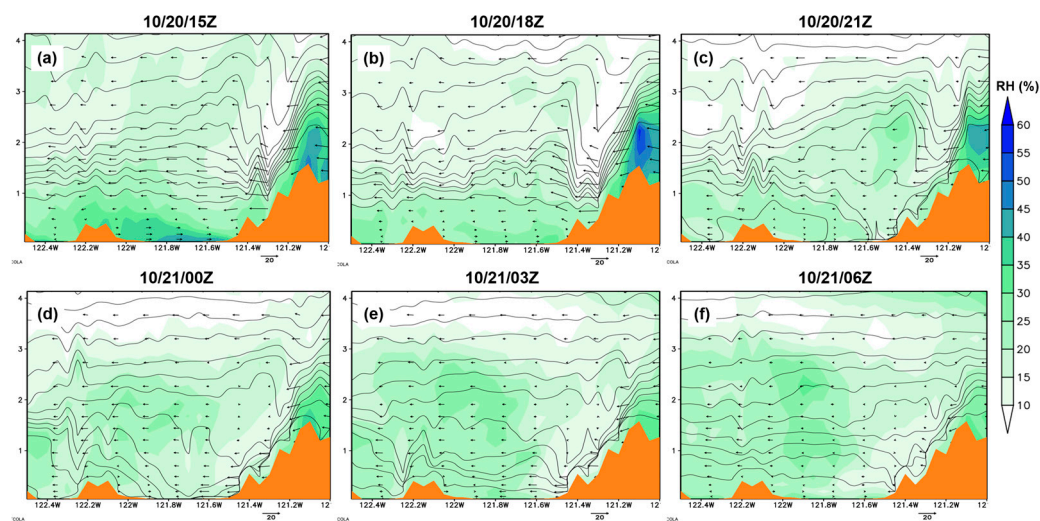

Figure A3. Vertical cross-section from the WRF (d03) simulation of RH (shaded; %), isentropes (contour lines; K), and wind barbs from 10/20/15Z to 10/21/06Z. The cross-section is along line CD (denoted in Figure 11). Strong winds are seen at the lee side of the Sierra Nevada, which transports dry air over the Central Valley of California to the East Bay Hills area (Panels **a**,**b**). Panels (**c**–**f**) illustrate that wind speeds decreased, revealing weaker winds on the leeside of the Sierra Nevada when the fire was contained.

References

1. Huang, C.; Lin, Y.-L.; Kaplan, M.L.; Charney, J.J. Synoptic-scale and mesoscale environments conducive to forest fires during the October 2003 extreme fire event in southern California. *J. Appl. Meteorol. Climatol.* **2009**, *48*, 553–579. [CrossRef]
2. Smith, C.M.; Hatchett, B.J.; Kaplan, M.L. Characteristics of Sundowner winds near Santa Barbara, California, from a dynamically downscaled climatology: Environment and effects near the surface. *J. Appl. Meteorol. Climatol.* **2018**, *57*, 589–606. [CrossRef]
3. Kaplan, M.L.; Tilley, J.S.; Hatchett, B.J.; Smith, C.M.; Walston, J.M.; Shourd, K.N.; Lewis, J.M. The Record Los Angeles Heat Event of September 2010: 1. Synoptic-Scale-Meso-β-Scale Analyses of Interactive Planetary Wave Breaking, Terrain- and Coastal-Induced Circulations. *J. Geophys. Res. Atmos.* **2017**, *122*, 10–729. [CrossRef]

4. Sharples, J.J. An overview of mountain meteorological effects relevant to fire behavior and bushfire risk. *Int. J. Wildland Fire* **2009**, *18*, 737–754. [CrossRef]

5. Smith, C.; Hatchett, B.J.; Kaplan, M. A surface observation-based climatology of Diablo-like winds in California's wine country and western Sierra Nevada. *Fire* **2018**, *1*, 25. [CrossRef]

6. Routley, J.G. *East Bay Hills Fire Oakland-Berkeley, California*; United States Fire Administration: Emmitsburg, MD, USA, 1991.

7. Brewer, M.J.; Clements, C.B. The 2018 Camp Fire: Meteorological Analysis Using In Situ Observations and Numerical Simulations. *Atmosphere* **2019**, *11*, 47. [CrossRef]

8. Coen, J.L.; Schroeder, W.; Quayle, B. The Generation and Forecast of Extreme Winds during the Origin and Progression of the 2017 Tubbs Fire. *Atmosphere* **2018**, *9*, 462. [CrossRef]

9. Srock, A.F.; Charney, J.J.; Potter, B.E.; Goodrick, S.L. The hot-dry-windy index: A new fire weather index. *Atmosphere* **2018**, *9*, 279. [CrossRef]

10. Simard, A.J.; Haines, D.A.; Blank, R.W.; Frost, J.S. *The Mack Lake Fire. General Technical Report NC-83*; US Dept. of Agriculture, Forest Service, North Central Forest Experiment Station: St. Paul, MN, USA, 1983; Volume 83.

11. Haines, D.A. A lower atmospheric severity index for wildland fire. *Natl. Weather Dig.* **1988**, *13*, 23–27.

12. Pechony, O.; Shindell, D.T. Fire parameterization on a global scale. *J. Geophys. Res. Atmos.* **2009**, *114*, D16. [CrossRef]

13. Clark, T.L.; Peltier, W.R. Critical level reflection and the resonant growth of nonlinear mountain waves. *J. Atmos. Sci.* **1984**, *41*, 3122–3134. [CrossRef]

14. Smith, R.B. On severe downslope winds. *J. Atmos. Sci.* **1985**, *42*, 2597–2603. [CrossRef]

15. Klemp, J.B.; Lilly, D.K. The dynamics of wave-induced downslope winds. *J. Atmos. Sci.* **1975**, *32*, 320–339. [CrossRef]

16. Peltier, W.R.; Clark, T.L. The Evolution and Stability of Finite Amplitude Mountain Waves. Part II: Surface Wave Drag and Severe Downslope Windstorms. *J. Atmos. Sci.* **1979**, *36*, 1498–1529.

17. Long, R.R. Some aspects of the flow of stratified fluids. Part II. Experiments with a two-fluid system. *Tellus* **1954**, *6*, 97–115. [CrossRef]

18. Durran, D.R. Another look at downslope windstorms. Part I: The development of analogs to supercritical flow in an infinitely deep, continuously stratified fluid. *J. Atmos. Sci.* **1986**, *43*, 2527–2543. [CrossRef]

19. Lilly, D.K. A severe downslope windstorm and aircraft turbulence event induced by a mountain wave. *J. Atmos. Sci.* **1978**, *35*, 59–77. [CrossRef]

20. Park, J.-R.; Kim, J.-H.; Shin, Y.-S.; Kim, S.-H.; Chun, H.-Y.; Jang, W.; Tsai, C.-L.; Lee, G. A numerical simulation of a strong windstorm event in the Taebaek Mountain Region in Korea during the ICE-POP 2018. *Atmos. Res.* **2022**, *272*, 106158. [CrossRef]

21. Lin, Y.-L.; Wang, T.A. Flow regimes and transient dynamics of two-dimensional stratified flow over an isolated mountain ridge. *J. Atmos. Sci.* **1996**, *53*, 139–158. [CrossRef]

22. Gronoff, G.; Arras, P.; Baraka, S.; Bell, J.M.; Cessateur, G.; Cohen, O.; Curry, S.M.; Drake, J.J.; Elrod, M.; Erwin, J.; et al. Atmospheric escape processes and planetary atmospheric evolution. *J. Geophys. Res. Space Phys.* **2020**, *125*, e2019JA027639. [CrossRef]

23. Gilmann, C.; Way, M.J.; Avice, G.; Breuer, D.; Golabek, G.J.; Höning, D.; Krissansen-Totton, J.; Lammer, H.; O'Rourke, J.G.; Persson, M.; et al. The long-term evolution of the amtosphere of Venus: Processes and feedback mechanisms. *Space Sci. Rev.* **2022**, *218*, 56. [CrossRef]

24. Ma, M.; Cao, J.; Tong, D.; Zheng, B.; Zhao, Y. Spatial and temporalevolution of future atmospheric reactive nitrogen deposition in China under different climate change mitigation strategies. *EGUsphere* **2024**. [CrossRef]

25. Skamarock, W.C.; Klemp, J.B.; Dudhia, J.; Gill, D.O.; Barker, D.; Duda, M.G.; Huang, X.-Y.; Wang, W.; Powers, J.G. A Description of the Advanced Research WRF Version 3. *Univ. Corp. Atmos. Res.* **2008**, *475*, 10-5065. [CrossRef]

26. Wiles, J.T.; Lin, Y.-L.; Kaplan, M.L. Multi-Scale Numerical Simulations of the Synoptic Environment, Diablo Windstorm, and Wildfire Formation Mechanisms for the Tubbs Fire (2017). *Meteorol. Atmos. Phys.* **2024**, *136*, 5. [CrossRef]

27. Lin, Y.-L.; Farley, R.D.; Orville, H.D. Bulk parameterization of the snow field in a cloud model. *J. Appl. Meteorol. Climatol.* **1983**, *22*, 1065–1092. [CrossRef]

28. Kain, J.S. The Kain-Fritsch convective parameterization: An update. *J. Appl. Meteorol.* **2004**, *43*, 170–181. [CrossRef]

29. Janjic, Z.I. The step-mountain Eta coordinate model: Further developments of the convection, viscous layer, and turbulence closure schemes. *Mon. Weather Rev.* **1994**, *122*, 927–945. [CrossRef]

30. Mlawer, E.J.; Taubman, S.J.; Brown, P.D.; Iacono, M.J.; Clough, S.A. Radiative transfer for inhomogeneous atmospheres: RRTM, a validated correlated-k model for the longwave. *J. Geophys. Res. Atmos.* **1997**, *102*, 16663–16682. [CrossRef]

31. Iacono, M.J.; Delamere, J.S.; Mlawer, E.J.; Shephard, M.W.; Clough, S.A.; Collins, W.D. Radiative forcing by long-lived greenhouse gases: Calculations with the AER radiative transfer models. *J. Geophys. Res. Atmos.* **2008**, *113*, D13. [CrossRef]

32. Simpson, J.E. *Sea Breeze and Local Wind Systems*; Cambridge University Press: Cambridge, UK, 1994.

33. Physick, W.L.; Byron-Scott, R.A. Numerical Experiments on Sea Breeze Circulation. *Bound.-Layer Meteorol.* **1977**, *12*, 215–236. [CrossRef]

34. Steyn, D.G. Scaling the Vertical Structure of Sea Breezes. *Bound.-Layer Meteorol.* **2003**, *107*, 247–273. [CrossRef]

35. Oke, T.R. *Boundary Layer Climates*, 2nd ed.; Methuen: London, UK, 1987.

36. Hinestroza-Ramirez, J.E.; Rengifo-Castro, J.D.; Quintero, O.L.; Yarce Botero, A.; Rendon-Perez, A.M. Non-Parametric and Robust Sensitivity Analysis of the Weather Research and Forecast (WRF) Model in the Tropical Andes Region. *Atmosphere* **2023**, *14*, 686. [CrossRef]

37. Arregocés, H.A.; Rojano, R.; Restrepo, G. Sensitivity Analysis of Planetary Boundary Layer Schemes Using the WRF Model in Northern Colombia during the 2016 Dry Season. *Dyn. Atmos. Oceans* **2021**, *96*, 101261. [CrossRef]

38. US Department of Commerce; NOAA; NWS. The Marine Layer. In *NWS JetStream*; 2019. Available online: https://www.noaa.gov/jetstream/ocean/marine-layer (accessed on 12 August 2021).

39. National Oceanic and Atmospheric Administration (NOAA). "Tunnel" Wildfire Oakland-Berkeley Hills 20–23 October 1991. In *Natural Disaster Survey Report*; US Department of Commerce, NOAA, NWS: Washington, DC, USA, 1992. Available online: https://ggweather.com/firestorm/NWS_Report_Oak_Fire.pdf (accessed on 12 August 2021).

40. Stein, A.F.; Draxler, R.R.; Rolph, G.D.; Stunder, B.J.B.; Cohen, M.D.; Ngan, F. NOAA's HYSPLIT Atmospheric Transport and Dispersion Modeling System. *Bull. Am. Meteorol. Soc.* **2015**, *96*, 2059–2077. [CrossRef]

41. Rolph, G.; Stein, A.; Stunder, B. Real-Time Environmental Applications and Display System: READY. *Environ. Model. Softw.* **2017**, *95*, 210–228. [CrossRef]

42. Uccellini, L.W.; Johnson, D.R. The Coupling of Upper and Lower Tropospheric Jet Streaks and Implications for the Development of Severe Convective Storms. *Mon. Weather Rev.* **1979**, *107*, 682–703. [CrossRef]

43. Uccellini, L.W.; Kocin, P.J. The interaction of jet streak circulations during heavy snow events along the east coast of the United States. *Weather Forecast.* **1987**, *2*, 289–308. [CrossRef]

44. Lin, Y.-L. *Mesoscale Dynamics*; Cambridge University Press: Cambridge, UK, 2007. [CrossRef]

45. Scinocca, J.F.; Peltier, W.R. The instability of Long's stationary solution and the evolution toward severe downslope windstorm flow. Part I: Nested grid numerical simulations. *J. Atmos. Sci.* **1993**, *50*, 2245–2263. [CrossRef]

46. Woods, J.D. Wave-induced shear instability in the summer thermocline. *J. Fluid Mech.* **1968**, *32*, 791–800. [CrossRef]

47. Erickson, M.J.; Charney, J.J.; Colle, B.A. Development of a Fire Weather Index Using Meteorological Observations within the Northeast United States. *J. Appl. Meteorol. Climatol.* **2016**, *55*, 389–402. [CrossRef]